19. T. Kaneko *et al.*, *DNA Res.* **9**, 189 (2002).
20. V. Gonzalez *et al.*, *Proc. Natl. Acad. Sci. U.S.A.* **103**, 3834 (2006).
21. J. P. Young *et al.*, *Genome Biol.* **7**, R34 (2006).
22. P. Roche, P. Lerouge, C. Ponthus, J. C. Promé, *J. Biol. Chem.* **266**, 10933 (1991).
23. J. Dénarié and F. Maillet, personal communication.
24. A. Costacurta, J. Vanderleyden, *Crit. Rev. Microbiol.* **21**, 1 (1995).
25. I. Lerouge, J. Vanderleyden, *FEMS Microbiol. Rev.* **26**, 17 (2002).
26. W. D'Haeze, M. Holsters, *Trends Microbiol.* **12**, 555 (2004).
27. J. A. Leigh, D. L. Coplin, *Annu. Rev. Microbiol.* **46**, 307 (1992).
28. J. Dénarié, B. Bergeron, in *Symbiotic Nitrogen Fixation*, P. S. Nutman, Ed. (Cambridge Univ. Press, Cambridge, 1975), pp. 47–61.
29. H. M. Meade, S. R. Long, G. B. Ruvkun, S. E. Brown, F. M. Ausubel, *J. Bacteriol.* **149**, 114 (1982).
30. M. J. Sadowsky, K. Rostas, P. R. Sista, H. Bussey, D. P. S. Verma, *Arch. Microbiol.* **144**, 334 (1986).
31. J. S. So *et al.*, *Mol. Gen. Genet.* **207**, 15 (1987).
32. E. J. Patriarca, R. Tate, M. Iaccarino, *Microbiol. Mol. Biol. Rev.* **66**, 203 (2002).
33. A. Schluter, M. Nohlen, M. Kramer, R. Defez, U. B. Priefer, *Microbiology* **146**, 2987 (2000).
34. C. E. Pankhurst, E. A. Schwinghamer, *Arch. Microbiol.* **100**, 219 (1974).
35. K. D. Noel, R. J. Diebold, J. R. Cava, B. A. Brink, *Arch. Microbiol.* **149**, 499 (1988).
36. M. Collavino, P. M. Riccillo, D. H. Grasso, M. Crespi, M. Aguilar, *Mol. Plant Microbe Interact.* **18**, 742 (2005).
37. J. D. Newman, R. J. Diebold, B. W. Schultz, K. D. Noel, *J. Bacteriol.* **176**, 3286 (1994).
38. D. B. Sturtevant, B. J. Taller, *Plant Physiol.* **89**, 1247 (1989).
39. L. Boiero *et al.*, *Appl. Microbiol. Biotechnol.* **74**, 874 (2007).
40. J. B. Cooper, S. R. Long, *Plant Cell* **6**, 215 (1994).
41. J. D. Murray *et al.*, *Science* **315**, 101 (2007).
42. L. Tirichine *et al.*, *Science* **315**, 104 (2007).
43. W. G. Reeve *et al.*, *Microbiology* **145**, 1307 (1999).
44. M. A. Jacobs *et al.*, *Proc. Natl. Acad. Sci. U.S.A.* **100**, 14339 (2003).
45. We would like to thank M. Boursot and C. Chaintreuil for technical help, S. Sylla and I. Ndoye for providing *Aeschynomene* seeds, and the DOE's Joint Genome Institute production sequencing team. The sequencing work on ORS278 was performed at Genoscope, Evry, France and supported by the Consortium National de la Recherche en Génomique (CNRG) and MRT/ACI IMPBio2004. A portion of the BTAi1 sequencing work was performed under the auspices of the U.S. Department of Energy's Office of Science, Biological and Environmental Research Program, by the University of California, Lawrence Livermore National Laboratory, Lawrence Berkeley National Laboratory, and Los Alamos National Laboratory. This work was supported, in part, from grants from the French Agence Nationale de la Recherche (ANR Blanc), and grant 2004-35604-14708 from the National Research Initiative of the Cooperative State Research, Education, and Extension Service, U.S. Department of Agriculture (USDA) (to D.E., M.S., and G.S.). Sequences of the entire genomes of *Bradyrhizobium* sp. ORS278 and BTAi1 have been submitted to the EMBL database under accession number CU234118, and to the GenBank database under accession numbers CP000494 (chromosome) and CP000495 (plasmid), respectively. Expert annotation data and comparative analysis results are publicly available via the MaGe interface in the RhizoScope relational database https://www.genoscope.cns.fr/agc/mage. Strain BTAi1 has been deposited in the American Type Culture Collection under accession number BAA-1182.

Supporting Online Material
www.sciencemag.org/cgi/content/full/316/5829/1307/DC1
Materials and Methods
Figs. S1 to S4
Tables S1 to S3

4 January 2007; accepted 12 April 2007
10.1126/science.1139548

REPORTS

Quantum Register Based on Individual Electronic and Nuclear Spin Qubits in Diamond

M. V. Gurudev Dutt,[1]* L. Childress,[1]* L. Jiang,[1] E. Togan,[1] J. Maze,[1] F. Jelezko,[2] A. S. Zibrov,[1] P. R. Hemmer,[3] M. D. Lukin[1]†

The key challenge in experimental quantum information science is to identify isolated quantum mechanical systems with long coherence times that can be manipulated and coupled together in a scalable fashion. We describe the coherent manipulation of an individual electron spin and nearby individual nuclear spins to create a controllable quantum register. Using optical and microwave radiation to control an electron spin associated with the nitrogen vacancy (NV) color center in diamond, we demonstrated robust initialization of electron and nuclear spin quantum bits (qubits) and transfer of arbitrary quantum states between them at room temperature. Moreover, nuclear spin qubits could be well isolated from the electron spin, even during optical polarization and measurement of the electronic state. Finally, coherent interactions between individual nuclear spin qubits were observed and their excellent coherence properties were demonstrated. These registers can be used as a basis for scalable, optically coupled quantum information systems.

Quantum registers are controllable quantum systems composed of several qubits. They form fundamental building blocks for quantum information science and can be connected into useful communication and computation systems, for example, via quantum optical channels (*1*–*9*). A useful register must support high-fidelity local operations between its qubits as well as permit excellent isolation of the qubits from each other and from the external environment. Over the past few years, quantum registers consisting of a few interacting trapped ions with exceptional coherence properties have been implemented experimentally (*10*, *11*), and the first steps toward optical interconnections have been taken (*12*, *13*). We report on the realization of a quantum register in a room-temperature solid by means of controlled manipulation of individual electron and nuclear spins.

Our approach makes use of coherent manipulation of the electron spin associated with individual nitrogen vacancy (NV) centers in diamond (*14*–*18*). The NV center has a long-lived spin triplet in its electronic ground state (*14*) that can be initialized, manipulated, and measured using microwave and optical excitation (Fig. 1A) (*15*). In pure samples, the electron spin acts as a sensitive magnetic probe of the local environment. The electron spin dynamics is governed by interactions with spin-½ ^{13}C nuclei (present in 1.1% natural abundance) in the diamond lattice (Fig. 1B). Although such a nuclear spin environment normally causes dephasing of electron spin qubits (*19*, *20*), we show that if properly controlled it also provides a very useful resource. Certain proximal nuclei, by virtue of their stronger hyperfine interaction and enhanced magnetic moment, can be distinguished from each other and from the rest of the environment (*21*), allowing us to individually address single nuclear spins and to use the resulting electron-nuclear coupled systems as few-qubit registers.

Although nuclear spins are well known for their long coherence times (*22*), conventional techniques for probing them require the use of macroscopic spin ensembles to obtain measurable signals (*23*, *24*). Coherent oscillations of a single nuclear spin were observed in (*25*), using a thermal state of a ^{13}C nuclear spin that was inextricably coupled by strong contact interactions with the nearest-neighbor NV electron spin. In contrast, we demonstrate a high degree of polarization (corresponding to an effective spin temperature below 1 μK) and control over an isolated nuclear spin that is coupled nonlocally to the electron spin. This results in coherence times

[1]Department of Physics, Harvard University, Cambridge, MA 02138, USA. [2]Physikalisches Institut, Universtität Stuttgart, Pfaffenwaldring 57, D-70550 Stuttgart, Germany. [3]Department of Electrical and Computer Engineering, Texas A&M University, College Station, TX 77843, USA.

*These authors contributed equally to this work.
†To whom correspondence should be addressed. E-mail: lukin@fas.harvard.edu

that are at least three orders of magnitude longer, and allows independent control over the electron and nuclear spin qubits, which is essential for scalable applications.

Individual nuclear spins in the diamond lattice can be manipulated by combining control over an NV electronic spin with a coherent mapping between electron and nuclear spin states. Consider a system involving an NV electron spin interacting with a single proximal ^{13}C nuclear spin (Fig. 1C). When the electron is in the $m_s = 0$ state, the hyperfine interaction vanishes. When the electron is in the $m_s = 1$ state, the hyperfine interaction introduces a splitting ω_I between the nuclear spin states $\{|1, \downarrow\rangle, |1, \uparrow\rangle\}$; hence, we can selectively flip the electron spin state conditional on the nuclear spin. If we apply a weak magnetic field perpendicular to the nuclear spin quantiza-

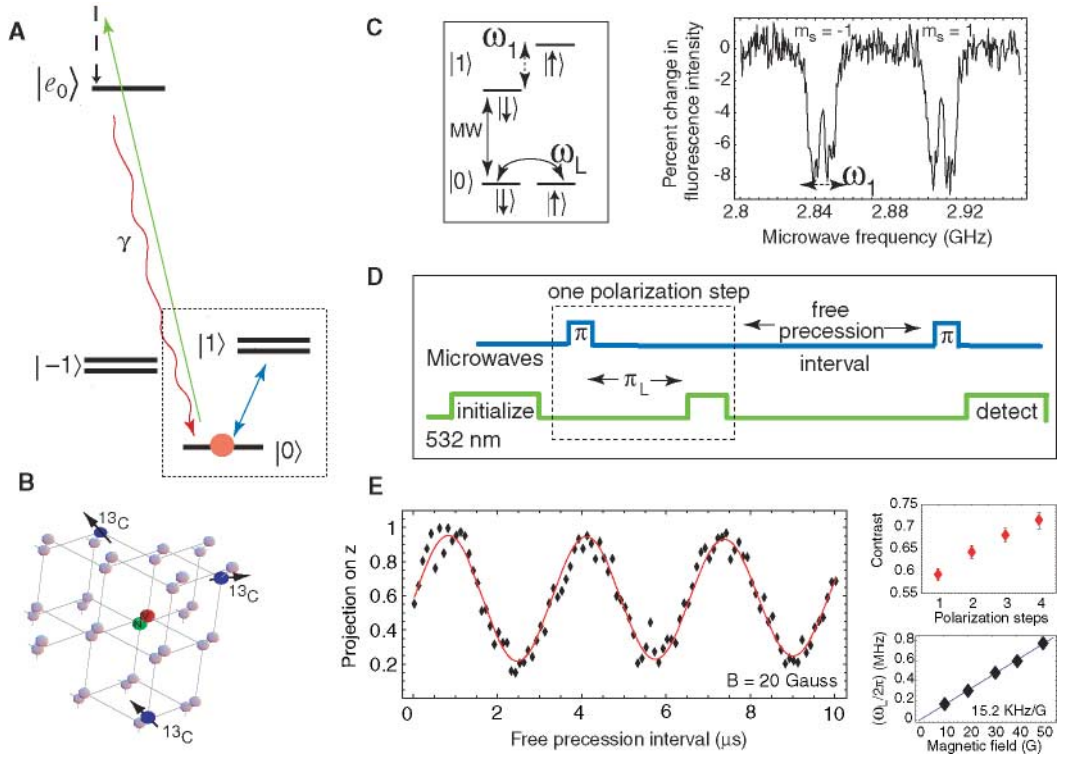

Fig. 1. Isolating, addressing, and reading out single electron and nuclear spins in the register. (**A**) Level diagram for the coupled spin system formed by the NV electron spin and a nearby ^{13}C nuclear spin. Optical transitions of the NV center are used to polarize and measure the electron spin state of the NV. (**B**) Illustration of the ^{13}C environment near the NV center that is used to create the register. (**C**) A single electron spin transition $|0\rangle$ to $|1\rangle$ is addressed with resonant microwaves (MW), and hyperfine structure associated with the ^{13}C spin states $|\uparrow\rangle$, $|\downarrow\rangle$ can be resolved within this transition. (**D**) Experimental pulse sequence. As described in the text, we create and measure the nuclear spin polarization in $|\downarrow\rangle$ via the electron spin. (**E**) Nuclear free precession in a ~20-G magnetic field. Top right inset: By increasing the number of polarization steps, a higher contrast for the nuclear free precession signal is obtained. Four polarization steps were used for the data shown. Bottom right inset: Observed Larmor frequency as a function of magnetic field, approximately oriented along $\hat{x} - (\hat{z}/4)$, where $\hat{z}$ is the NV axis.

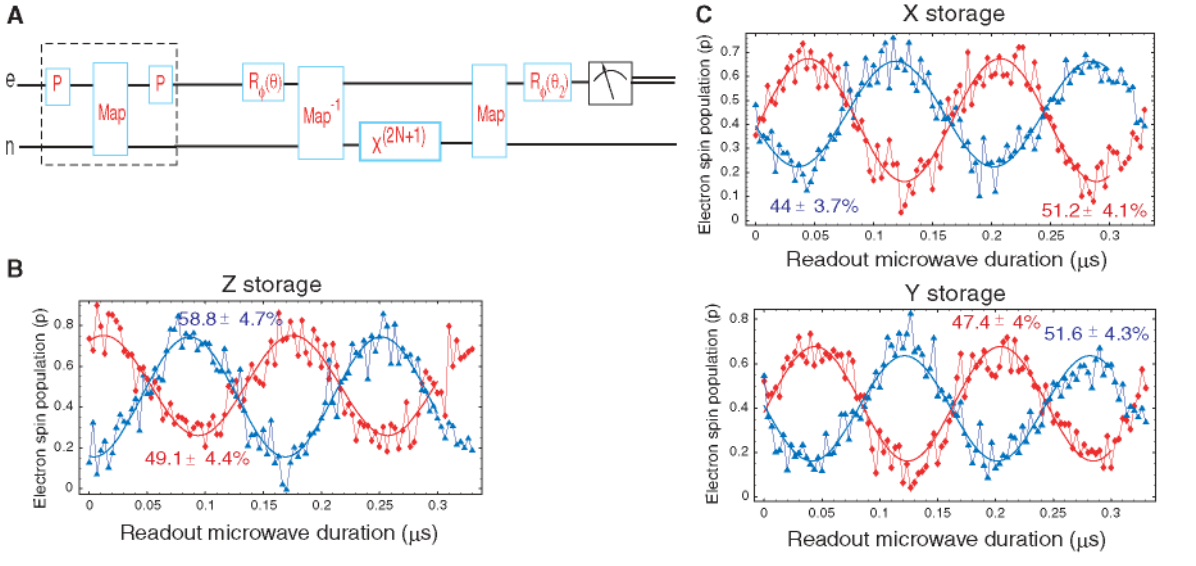

Fig. 2. Storage and retrieval of electron spin coherence in a single nuclear spin. (**A**) Experimental sequence. A single nuclear spin is prepared in the state $|\downarrow\rangle$, after which an electron spin state is created by appropriate microwave pulses $R_\phi(\theta)$, where θ is the rotation angle and $\phi = (0, \pi/2)$ is the phase of the qubit rotation relative to the storage step. The electron spin state is then mapped onto the nuclear spin and is mapped back after an interval $(2N + 1)\pi_L$. The resulting electron spin state is read out by driving electron spin nutations with $R_\phi(\theta_2)$, where θ_2 is varied. (**B** and **C**) Observed electron spin nutations after storage of different electron spin states. X storage refers to storage of the electron spin state $(1/\sqrt{2})(|0\rangle \pm |1\rangle)$, Y storage is $(1/\sqrt{2})(|0\rangle \pm i|1\rangle)$, and Z storage measures the population storage, $\{|0\rangle, |1\rangle\}$. The total time is $3\pi_L \sim 2.4\ \mu s > T_{2e}^*$ between creation of the electron spin state and measurement.

tion axis, the nuclear spin precesses at the Larmor frequency ω_L when the electron spin is in the $m_s = 0$ state. When the electron spin is in $m_s = 1$, the large hyperfine splitting ω_1 prevents Larmor precession. By selectively driving a π pulse on one hyperfine transition $|0, \downarrow\rangle \leftrightarrow |1, \downarrow\rangle$, and then waiting for a time $\tau = \pi/\omega_L$ (denoted as π_L), we can map a nuclear spin superposition onto the electron spin, $|0\rangle \otimes (\alpha|\downarrow\rangle + \beta|\uparrow\rangle) \rightarrow |\downarrow\rangle \otimes (\alpha|1\rangle + \beta|0\rangle)$ (Fig. 1D). This mapping gate (*Map*) allows complete control over the specific, individual nuclear spins because of their unique hyperfine splitting and Larmor frequencies.

The present experiments were carried out with the use of a setup described in (*21*). The nuclear spin is polarized by first preparing the electron spin state $|0\rangle$ by means of optical pumping with 532-nm light (*15*, *16*), mapping the initial incoherent mixture of nuclear spin states onto the electron spin, and then applying a pulse of 532-nm light sufficient to repolarize the electron spin into $|0\rangle$. Ideally, this pumping step results in the system being prepared in the state $|0, \downarrow\rangle$. In practice it can be repeated several times to further increase nuclear spin polarization. After a variable precession time, the nuclear spin state can be measured by mapping it onto the electron spin, which exhibits state-selective fluorescence. The observed contrast of $C \sim 70\%$ achievable with four pumping steps (Fig. 1E) indicates that we prepare and read out the nuclear spin state with an overall fidelity $F = (1 + C)/2$ (*10*) greater than 85% (*26*). The enhancement of the gyromagnetic ratio $(\gamma_n/2\pi) = 15.2$ kHz/G over the bare ^{13}C nuclear spin arises from interactions with the proximal electron spin, yielding a unique "chemical shift" (*23*) for the specific nuclear spin, depending on its relative position from the NV center (*21*). This is the key physical mechanism allowing for isolation of individual nuclear spin qubits and control of few-qubit registers.

Having established a procedure to reliably initialize and read out individual nuclear spins in the electron environment, we carried out a nontrivial quantum operation with the two-qubit register: storage and retrieval of an arbitrary electronic qubit in a nuclear qubit with high fidelity. This operation is particularly important in light of proposed protocols for quantum information processing (*6*–*9*). The experimental procedure is illustrated in Fig. 2A. After polarizing the nuclear spin, we created an electron spin state in one of three bases: $\{X_\pm = (1/\sqrt{2})(|0\rangle \pm |1\rangle)$, $Y_\pm = (1/\sqrt{2})(|0\rangle \pm i|1\rangle)$, $Z_{0,1} = \{|0\rangle, |1\rangle\}\}$. The electron spin was then stored in the nuclear spin via the inverse mapping gate (Map^{-1}), where it was allowed to remain for a time $(2N + 1)\pi_L$ before retrieval via the gate *Map*. We then observed the retrieved coherence (for X or Y storage) or population (for Z storage) by driving electron spin nutations and recording their contrast relative to nutations of a fully polarized electron spin. The overall fidelity of the memory is $F = (1 + \langle C \rangle)/2$, where $\langle C \rangle$ is the average contrast for the six measurements; we find $F = 75 \pm 1.3\%$ (*26*), which exceeds the classical limit (*27*) of $F_c = \frac{2}{3}$.

To investigate the degree of independent control over the two coupled qubits, we studied the nuclear spin evolution under the optical excitation used to polarize and measure the electron spin qubit (Fig. 3). We prepared a nuclear spin state $(|\uparrow\rangle + |\downarrow\rangle)/\sqrt{2}$ or $|\uparrow\rangle$ by initializing into $|\downarrow\rangle$ and allowing the spin to precess for either $\pi_L/2$ or π_L. A pulse of 532-nm light was then applied, which could dephase or depolarize the nuclear spin state, resulting in reduced contrast of the nuclear free precession signal (Fig. 3A). As we increased the duration of the 532-nm light pulse, we found that the nuclear spin precession signal decayed much more slowly than did the electron spin. In particular, hardly any nuclear spin dephasing was visible for light pulses of ~140 ns (dashed line in Fig. 3B) sufficient to completely polarize the electron spin. Furthermore, the illuminated nuclear spin decay depended on the magnetic field (Fig. 3C). Whereas a few scattered photons completely decohered the electron spin, at low magnetic fields the nuclear precession was unaffected by a large number ($\sim 10^3$) of scattered optical photons. This insensitivity is critical for optical scaling (*7*, *9*) because many optical cycles may be required to establish entanglement between the registers (*12*, *13*).

The dephasing under optical illumination shown in Fig. 3 can be qualitatively understood as arising from different nuclear Larmor precession rates in the ground and optically excited electronic states. The nuclear gyromagnetic ratio is strongly enhanced by hyperfine interactions with the electron spin, which depends on the electron spatial distribution (*21*). Excited electron orbital states can thus lead to different nuclear gyromagnetic ratios. Under optical illumination, the system makes transitions between orbital states with different nuclear spin precession rates. To estimate the resulting nuclear spin dephasing, we suppose that optical excitation induces transitions at a rate $1/\tau_r$, much faster than the difference of the state-dependent nuclear spin precession frequencies $\delta\omega$. After each transition, the nuclear spin picks up a small random phase $\phi \sim \delta\omega\tau_r$. Variations in this random phase give rise to dephasing at a rate $\sim \delta\omega^2\tau_r$, much smaller than the illuminated electron spin dephasing rate $\sim 1/\tau_r$. Because $\delta\omega$ is proportional to the magnetic field for states with $m_s = 0$, it may be possible to almost completely decouple electron and nuclear spins by switching the magnetic field to zero during free evolution.

Finally, we explored the coherence properties of the nuclear spin quantum memory. In contrast to the electron spin, which dephases on a time scale $T_{2e}^* \sim 1$ μs for this NV center, the nuclear spin free precession signal persisted out to ~0.5 ms ($T_{2n}^* = 495 \pm 30$ μs in Fig. 4A). Characteristic collapses and revivals in the data correspond to coherent interactions between individual nuclear spins. The nuclear spins can be decoupled using a Hahn echo (or spin-echo) sequence (*23*), which consists of $(\pi/2)_n$-τ-π_n-τ'-$(\pi/2)_n$, where $(\pi)_n$ represents a pulse that flips the nuclear spin, and τ and τ' are durations of free evolution (Fig. 4C). We accomplished the nuclear π-pulse by exciting the system into the $m_s = 1$ manifold, where the large hyperfine splitting rapidly introduces a phase between the nuclear spin states. Viewed in the orthogonal $m_s = 0$ eigenbasis, this constitutes the

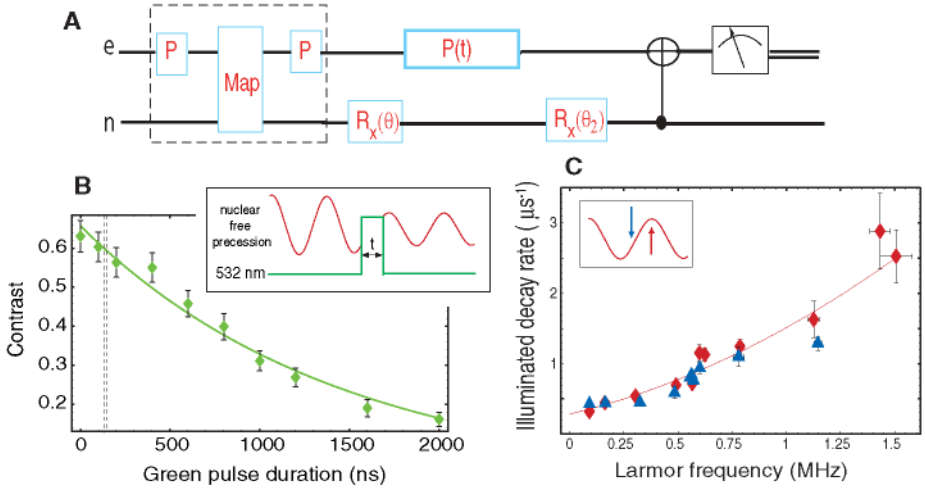

Fig. 3. Probing the isolation of a nuclear spin qubit under optical illumination. (**A**) Experimental sequence as explained in text. (**B**) Decay of illuminated nuclear spin free precession. When illuminated by approximately half the saturation intensity at 532 nm for the NV optical transition, the nuclear spin signal decays on a time scale of 1.5 ± 0.1 μs. For comparison, the polarization rate for the electron spin (under the same conditions) is 140 ± 6 ns, shown by the dashed lines. (**C**) Illuminated decay rate as a function of magnetic field. The decay rate does not depend strongly on whether we apply green light when the nuclear spin is in its polarized state $|\uparrow\rangle$ (red points) or in a superposition state $(1/\sqrt{2})(|\uparrow\rangle + |\downarrow\rangle)$ (blue points), as illustrated in the inset. The data are fitted to the function $(a + b\omega_L)^2$.

population nutations required to effect a π_n pulse (*26*). As shown in Fig. 4D, the spin echo sequence extended the coherence time far beyond the values obtained from free evolution. Specifically, we observed no evidence of echo decay on the time scales accessible in our present experiments, limited by long averaging times, which suggests that T_2 of our nuclear spin qubit is well above 20 ms.

These results can be understood by considering the interactions between the observed ^{13}C nuclear spin ($\mathbf{I}_1$) with other ^{13}C nuclear spins $\mathbf{I}_j$. Let us first consider only one nearby spin $\mathbf{I}_2$: The Hamiltonian in the secular approximation is given by $H = \omega_L{}^1 I_{1,z} + \omega_L{}^2 I_{2,z} + \beta I_{1,z} I_{2,z}$, where $\omega_L{}^{1,2}$ are the Larmor frequencies of the two spins, and β is the effective dipole-dipole coupling between nuclei (*26*). As a result of the different Larmor frequencies caused by the different interactions with the NV electronic spin, these nuclear spins are not involved in flip-flop processes with each other or with the rest of the nuclear spin environment. Thus, the nuclear interaction only results in energy shifts $\pm\beta/4$ of $\mathbf{I}_1$ that depend on the state of $\mathbf{I}_2$, leading to the observed coherent modulation in the free precession (Fig. 4A) for $|\beta|/2\pi \sim 7.2$ kHz. Interactions with the next nearest spin $\mathbf{I}_3$ will similarly result in free precession collapse (and revival) on a longer time scale, etc. (fig. S1). This theoretical model predicts that the nuclear interactions introduce only static energy shifts that are easily refocused by the spin-echo sequence. The resulting nuclear spin coherence is greatly enhanced relative to the electron spin (*21*), consistent with the much weaker interactions of $\mathbf{I}_1$ with the surrounding environment. Further confirmation of the theoretical model comes from the observed dependence of the coherent coupling (modulation) rate on the orientation of the magnetic field (Fig. 4B), which illustrates the anisotropic character of the electron-mediated nuclear dipole-dipole interaction (*26*).

These observations indicate that controlled manipulation of a few coupled nuclear spin qubits is possible in a room-temperature solid-state system, with coherence times that can approach seconds when advanced nuclear magnetic resonance techniques are used (*23*). In addition to the direct coupling between the nuclear spins demonstrated here, the number of distinct controllable nuclear spins in the register can be increased by selecting NV centers with a few proximal ^{13}C spins (*21*), or by creating NV centers through controlled implantation of $I = ½$ ^{15}N ions (*28*). Such registers provide a starting point for a realization of a quantum network in which qubits can be encoded and manipulated in nuclear spins via magnetic resonance techniques (*23*), whereas long-range entanglement between electron spins at arbitrary locations can be created optically (*6*–*9*, *29*) with techniques now explored for atoms and ions (*12*, *13*). Recently, the radiatively broadened lines and spin-dependent optical transitions required for realization of these techniques were demonstrated in diamond (*30*, *31*). Few-qubit registers can provide powerful tools for scalable quantum information systems even in the presence of realistic noise and losses that affect the long-range entanglement (*6*, *7*, *9*). Beyond specific applications in quantum information science, our measurements show that the electron spin can be used as a sensitive local magnetic probe that allows for a remark-

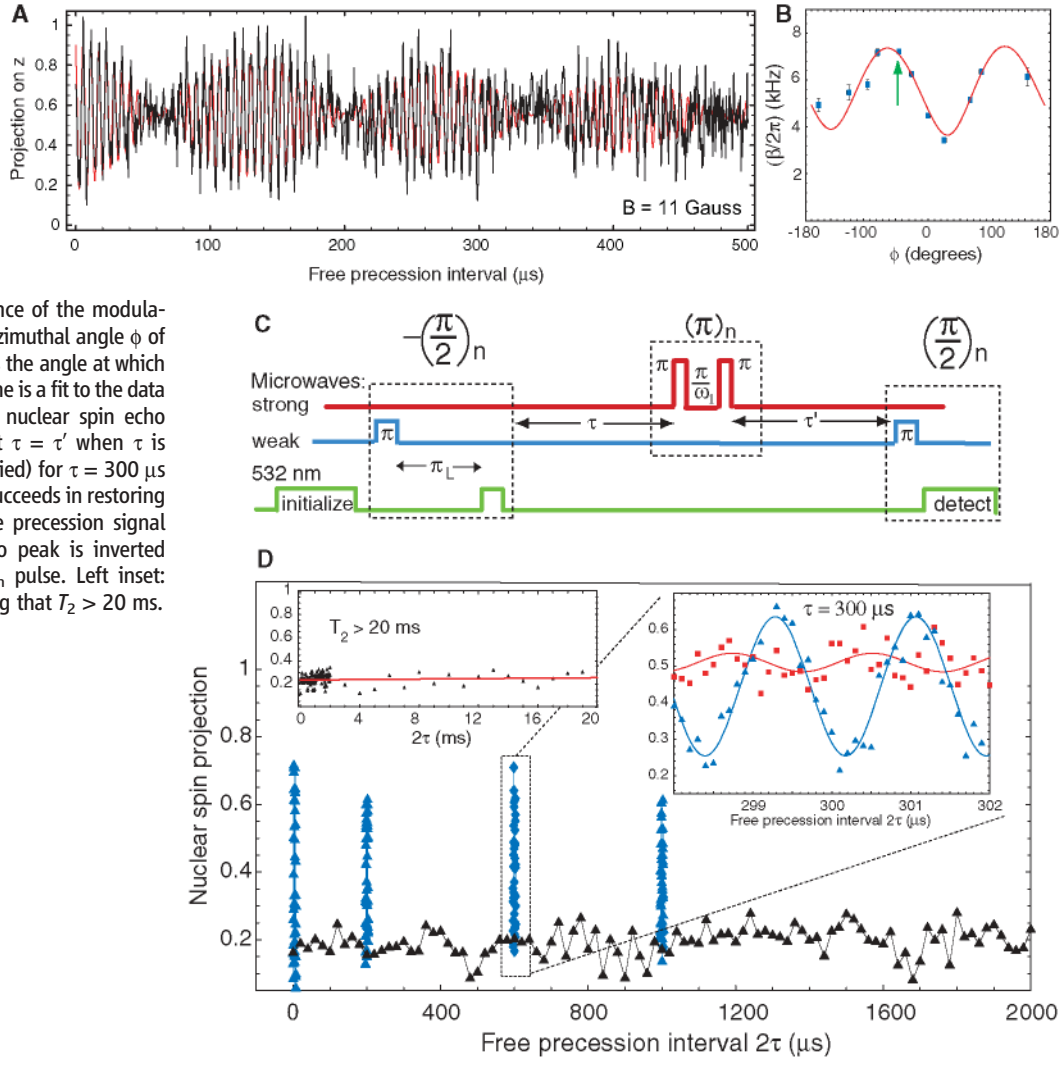

Fig. 4. Coherent dynamics of coupled nuclear spin qubits. (**A**) Long-time precession signal of a single nuclear spin in a magnetic field of 11 G. The data were fitted to the function $a + b\cos(\omega_L\tau)\cos(\beta\tau/2)\exp[-(\tau/T_{2n}{}^*)^2]$, where $\omega_L \sim 2\pi(172)$ kHz is the Larmor frequency, $\beta \sim 2\pi(7.2)$ kHz is the strength of the interaction with the nearby proximal nucleus, and $T_{2n}{}^*$ is the dephasing time. (**B**) Dependence of the modulation frequency (blue points) on the azimuthal angle ϕ of the magnetic field. The arrow denotes the angle at which the data in (A) were taken. The solid line is a fit to the data (*26*). (**C**) Experimental sequence for nuclear spin echo (*26*). (**D**) Main plot: Echo signal at $\tau = \tau'$ when τ is varied. Right inset: Echo data (τ' varied) for $\tau = 300$ μs (blue points) showing that the echo succeeds in restoring the coherence even though the free precession signal (red points) has vanished. The echo peak is inverted because we initially apply a $(-\pi/2)_n$ pulse. Left inset: Long-time echo signal, demonstrating that $T_2 > 20$ ms.

able degree of control over individual nuclear spins.

References and Notes

1. J. I. Cirac, P. Zoller, H. Mabuchi, H. J. Kimble, *Phys. Rev. Lett.* **78**, 3221 (1997).
2. A. Steane, D. Lucas, *Fortschr. Phys.* **48**, 839 (2000).
3. H. J. Briegel, W. Dür, J. I. Cirac, P. Zoller, *Phys. Rev. Lett.* **81**, 5932 (1998).
4. D. Gottesman, I. Chuang, *Nature* **402**, 390 (1999).
5. L. Duan, B. Blinov, D. Moehring, C. Monroe, *Quant. Inf. Comp.* **4**, 165 (2004).
6. S. C. Benjamin, D. E. Browne, J. Fitzsimons, J. J. L. Morton, *N. J. Phys.* **8**, 141 (2006).
7. L. Childress, J. M. Taylor, A. Sørensen, M. D. Lukin, *Phys. Rev. Lett.* **96**, 070504 (2006).
8. P. van Loock *et al.*, *Phys. Rev. Lett.* **96**, 240501 (2006).
9. L. Jiang, J. M. Taylor, A. S. Sorensen, M. D. Lukin, http://arxiv.org/abs/quant-ph/0703029 (2007).
10. D. Leibfried *et al.*, *Nature* **438**, 639 (2005).
11. H. Häffner *et al.*, *Nature* **438**, 643 (2005).
12. B. Blinov, D. L. Moehring, L. M. Duan, C. Monroe, *Nature* **428**, 153 (2004).
13. P. Maunz *et al.*, http://arxiv.org/abs/quant-ph/0608047 (2006).
14. J. Wrachtrup, S. Y. Kilin, A. P. Nizovtsev, *Opt. Spectrosc.* **91**, 429 (2001).
15. F. Jelezko, T. Gaebel, I. Popa, A. Gruber, J. Wrachtrup, *Phys. Rev. Lett.* **92**, 076401 (2004).
16. T. Gaebel *et al.*, *Nature Phys.* **2**, 408 (2006).
17. R. Hanson, F. Mendoza, R. J. Epstein, D. D. Awschalom, *Phys. Rev. Lett.* **97**, 087601 (2006).
18. R. J. Epstein, F. M. Mendoza, Y. K. Kato, D. D. Awschalom, *Nat. Phys.* **1**, 94 (2005).
19. J. R. Petta *et al.*, *Science* **309**, 2180 (2005); published online 1 September 2005 (10.1126/science.1116955).
20. F. H. L. Koppens *et al.*, *Nature* **442**, 766 (2006).
21. L. Childress *et al.*, *Science* **314**, 281 (2006); published online 13 September 2006 (10.1126/science.1131871).
22. B. Kane, *Nature* **393**, 133 (1998).
23. L. M. K. Vandersypen, I. L. Chuang, *Rev. Mod. Phys.* **76**, 1037 (2004).
24. C. Negrevergne *et al.*, *Phys. Rev. Lett.* **96**, 170501 (2006).
25. F. Jelezko *et al.*, *Phys. Rev. Lett.* **93**, 130501 (2004).
26. See supporting material on *Science* Online.
27. S. Massar, S. Popescu, *Phys. Rev. Lett.* **74**, 1259 (1995).
28. J. Rabeau *et al.*, *Appl. Phys. Lett.* **88**, 023113 (2006).
29. M. D. Lukin, P. R. Hemmer, *Phys. Rev. Lett.* **84**, 2818 (2000).
30. P. Tamarat *et al.*, *Phys. Rev. Lett.* **97**, 083002 (2006).
31. C. Santori *et al.*, *Phys. Rev. Lett.* **97**, 247401 (2006).

32. We thank P. Cappellaro, J. Doyle, N. Khaneja, C. Marcus, A. Mukherjee, J. Taylor, and J. Wrachtrup for many stimulating discussions and experimental help, and S. Prawer for providing high-purity diamond samples. Supported by NSF (CAREER and Physics at the Information Frontier), the Army Research Office, the Packard and Hertz Foundations, Deutsche Forschungsgemeinschaft grant SFB/TR21, and the European Commission (F.J.).

Supporting Online Material

www.sciencemag.org/cgi/content/full/316/5829/1312/DC1
Materials and Methods
SOM Text
Figs. S1 and S2
References

11 January 2007; accepted 11 April 2007
10.1126/science.1139831

Functional Quantum Nodes for Entanglement Distribution over Scalable Quantum Networks

Chin-Wen Chou, Julien Laurat, Hui Deng, Kyung Soo Choi, Hugues de Riedmatten,* Daniel Felinto,† H. Jeff Kimble‡

We demonstrated entanglement distribution between two remote quantum nodes located 3 meters apart. This distribution involves the asynchronous preparation of two pairs of atomic memories and the coherent mapping of stored atomic states into light fields in an effective state of near-maximum polarization entanglement. Entanglement is verified by way of the measured violation of a Bell inequality, and it can be used for communication protocols such as quantum cryptography. The demonstrated quantum nodes and channels can be used as segments of a quantum repeater, providing an essential tool for robust long-distance quantum communication.

In quantum information science (*1*), distribution of entanglement over quantum networks is a critical requirement for metrology (*2*), quantum computation (*3*, *4*), and communication (*3*, *5*). Quantum networks are composed of quantum nodes for processing and storing quantum states, and quantum channels that link the nodes. Substantial advances have been made with diverse systems toward the realization of such networks, including ions (*6*), single trapped atoms in free space (*7*, *8*) and in cavities (*9*), and atomic ensembles in the regime of continuous variables (*10*).

An approach of particular importance has been the seminal work of Duan, Lukin, Cirac, and Zoller (DLCZ) for the realization of quantum networks based on entanglement between single photons and collective excitations in atomic ensembles (*11*). Critical experimental capabilities have been achieved, beginning with the generation of nonclassical fields (*12*, *13*) with controlled waveforms (*14*) and extending to the creation and retrieval of single collective excitations (*15*–*17*) with high efficiency (*18*, *19*). Heralded entanglement with quantum memory, which is the cornerstone of networks with efficient scaling, was achieved between two ensembles (*20*). More recently, conditional control of the quantum states of a single ensemble (*21*–*23*) and of two distant ensembles (*24*) has also been implemented; the quantum states are likewise required for the scalability of quantum networks based on probabilistic protocols.

Our goal is to develop the physical resources that enable quantum repeaters (*5*), thereby allowing entanglement-based quantum communication tasks over quantum networks on distance scales much larger than those set by the attenuation length of optical fibers, including quantum cryptography (*25*). For this purpose, heralded number-state entanglement (*20*) between two remote atomic ensembles is not directly applicable. Instead, DLCZ proposed the use of pairs of ensembles (U_i,D_i) at each quantum node i, with the sets of ensembles $\{U_i\},\{D_i\}$ separately linked in parallel chains across the network (*11*). Relative to the state of the art in our previous work (*20*), the DLCZ protocol requires the capability for the independent control of pairs of entangled ensembles between two nodes.

In our experiment, we created, addressed, and controlled pairs of atomic ensembles at each of two quantum nodes, thereby demonstrating entanglement distribution in a form suitable both for quantum network architectures and for entanglement-based quantum communication schemes (*26*). Specifically, two pairs of remote ensembles at two nodes were each prepared in an entangled state (*20*), in a heralded and asynchronous fashion (*24*), thanks to the conditional control of the quantum memories. After a signal indicating that the two chains are prepared in the desired state, the states of the ensembles were coherently transferred to propagating fields locally at the two nodes. The fields were arranged such that they effectively contained two photons, one at each node, whose polarizations were entangled. The entanglement between the two nodes was verified by the violation of a Bell inequality. The effective polarization-entangled state, created with favorable scaling behavior, was thereby compatible with entanglement-based quantum communication protocols (*11*).

The architecture for our experiment is shown in Fig. 1. Each quantum node, L (left) and R (right), consists of two atomic ensembles, U (up) and D (down), or four ensembles altogether, namely (LU, LD) and (RU, RD), respectively. We first prepared each pair in an entangled state, in which one excitation is shared coherently, by using a pair of coherent weak write pulses to induce spontaneous Raman transitions $|g\rangle \rightarrow |e\rangle \rightarrow |s\rangle$ (bottom left, Fig. 1). The Raman fields $(1_{LU},1_{RU})$ from (LU, RU) were

Norman Bridge Laboratory of Physics 12-33, California Institute of Technology, Pasadena, CA 91125, USA.

*Present address: Group of Applied Physics, University of Geneva, Geneva 1211, Switzerland.
†Present address: Departamento de Física, Universidade Federal de Pernambuco, Recife-PE, 50670-901, Brazil.
‡To whom correspondence should be addressed. E-mail: hjkimble@caltech.edu